

# A general approach to flaw simulation in castings by superimposing projections of 3D models onto real X-ray images

Dennis Hahn and Domingo Mery

Departamento de Ingeniería Informática  
Universidad de Santiago de Chile  
Av. Ecuador 3659, Santiago de Chile  
EMail: dhahn@123.cl, dmery@ieec.org  
<http://www.diiinf.usach.cl/~dmery>

## ABSTRACT

In order to evaluate the sensitivity of defect inspection systems, it is convenient to examine simulated data. This gives the possibility to tune the parameters of the inspection method and to test the performance of the system in critical cases. In this paper, a practical method for the simulation of defects in radioscopic images of aluminium castings is presented. The approach simulates only the flaws and not the whole radioscopic image of the object under test. A 3D mesh is used to model a flaw with complex geometry, which is projected and superimposed onto real radioscopic images of a homogeneous object according to the exponential attenuation law for X-rays. The new grey value of a pixel, where the 3D flaw is projected, depends only on four parameters: a) the grey value of the original X-ray image without flaw; b) the linear absorption coefficient of the examined material; c) the maximal thickness observable in the radioscopic image; and d) the length of the intersection of the 3D flaw with the modelled X-ray beam, that is projected into the pixel. A simulation of a complex flaw modelled as a 3D mesh can be performed in any position of the castings by using the algorithm described in this paper. This allows the evaluation of the performance of defect inspection systems in cases where the detection is known to be difficult. In this paper, we show experimental results on real X-ray images of aluminium wheels, in which 3D flaws like blowholes, cracks and inclusions are simulated.

## 1. Introduction

Radioscopy is increasingly being used as a tool for non-destructive testing in industrial production. An example is the serial examination of cast light-alloy work pieces used in the car industry, like aluminium wheels and steering gears (Kosanetsky & Putzbach, 1996). The material defects occurring in the casting process such as cavities, gas, inclusions, and sponging must be detected to satisfy the safety requirements; consequently, it is necessary to check 100% of the parts. Since most defects are not visible, X-ray imaging is used for this task. An example of a radioscopic image is shown in Fig. 1.

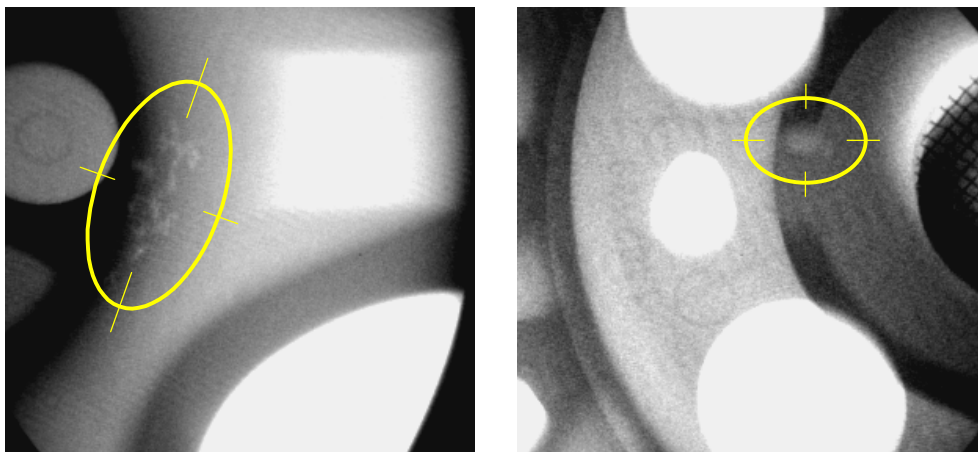


Fig. 1: Real flaws in radioscopic image of aluminium wheels.

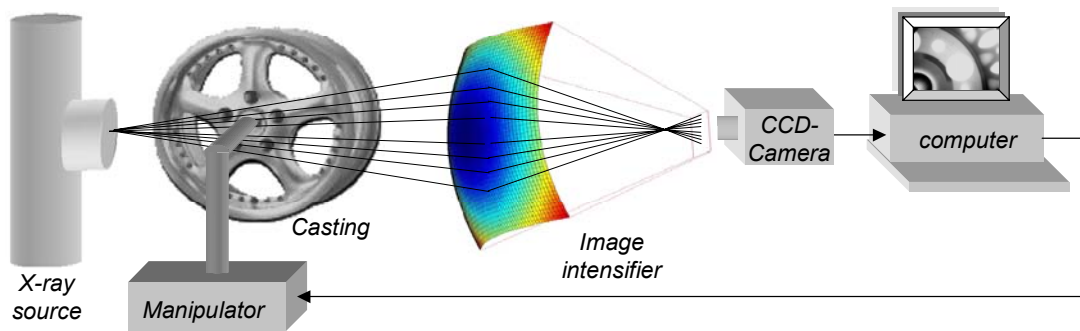


Fig. 2: Automated inspection system of die castings.

Over the past decades radioscopic systems have been introduced in the automotive manufacturing industry in order to detect flaws automatically without human interaction (Boerner & Strecker, 1988; Filbert et al, 1987; Heinrich, 1988). Over the years, they have not only increased quality through repeated objective inspections and improved processes, but have also increased productivity through decreased labour cost (Mery et al, 2001; Mery & Filbert, 2002).

An automated radioscopic system is schematically presented in Fig. 2. The inspection is typically performed in the five following steps: *i)* the *manipulator* places the casting in the desired position; *ii)* the *X-ray tube* generates an X-ray image of the casting via central projection; *iii)* the X-ray image is detected by the fluorescent entrance screen of the *image intensifier*, amplified and depicted onto a phosphor screen. The image intensifier converts the X-ray image to a visible radioscopic image; *iv)* the guided and focussed image is registered by the *CCD-camera*; and *v)* the *image processor* converts the analogue video signal, transferred by the CCD-camera, into a digital data stream. Digital image processing is used to improve and evaluate the radioscopic image.

In order to evaluate the performance of a method that inspects aluminium castings, it is convenient to examine simulated data. This evaluation gives the possibility of tuning the parameters of the inspection method and of testing how the method works in critical cases. Among the non-destructive testing and evaluation community there are two widespread approaches that produce this simulated data: *flaw superimposition* and *CAD models for casting and flaw*<sup>1</sup>.

**Flaw superimposition.** The first technique attempts to simulate flaws by superimposing circles with different Grey values onto real radioscopic images (Filbert et al, 1987; Heinrich, 1988; Hecker, 1995). This approach is quite simple, because it does not need any complex 3D model of the object under test nor of the flaw. Additionally, it offers a real radioscopic image with real disturbances (with simulated flaws). Nevertheless, the flaws simulated by this method differ significantly from the real ones. The reason being that a real flaw does not look like a projection of a disc. This method can only be used in restricted cases.

An improvement of this method can be obtained using the visualisation technique called *splatting* (Westover, 1990). In this technique the projection of a 3D flaw can be simulated, in which the projected flaw is assumed as a 2D Gaussian. The scale, position and orientation of the Gaussian are adjusted in order to obtain the desired projected flaw. Although this technique offers a better flaw simulation in comparison with the disc projection, its simulation corresponds to the projection of a 3D flaw, that differs considerably from real flaws as shown in (Mery, 2001).

**CAD models for casting and flaw.** The second approach makes a simulation of the entire X-ray imaging process (Tillack et al, 2000; Freud et al, 2000). In this approach, the characteristic of the X-

<sup>1</sup> There is another possibility -widely used within the non-destructive testing community- to obtain castings with known defects: drilling small holes in the casting (Bavendiek, 2001). However, this technique does not perform any image simulation.

ray source, the geometry and material properties of objects and their defects, as well as the imaging process itself are modelled and simulated independently. Complex objects and defect shapes can be simulated using CAD models. Although this approach offers excellent flexibility in setting the objects and flaws to be tested, it presents the following three disadvantages to the evaluation of the inspection methods' performance: *i*) the radioscopic image of the object under test is simulated (it would be better if we could count on real images with simulated flaws); *ii*) the simulation approach is only available when using a sophisticated computer package; *iii*) the computing time is very expensive.

In this paper, we address the above problems and propose an approach that only simulates the flaws (and not the whole radioscopic image of the object under test). This new method can be viewed as an improvement of the first mentioned technique and the 3D modelling for the flaws of the second one. In our approach, a 3D modelled flaw is projected and superimposed onto real radioscopic images of a homogeneous object according to the exponential attenuation law for X-rays (Kuchling, 1989). This idea was originally presented in (Mery, 2001), where a flaw was modelled as an ellipsoid. In this paper, we propose, however, a general model by using a polygonal mesh to simulate the flaws. This model suits best reality for any type of flaw.

The paper is organised as follows: In Section 2, a brief overview of the X-ray imaging process is presented. Section 3 describes our geometric model of the X-ray projection. The approach to simulate flaws in aluminium castings is outlined in Section 4. The results obtained on radioscopic images are described in Section 5. Finally, Section 6 gives concluding remarks.

## 2. X-Ray Imaging

Radiographic examination is a non-destructive testing technique, which uses X-ray radiation to detect material defects. In this examination method, radiation is passed through the material under test, and a detector senses the radiation intensity attenuated by the material. Thus, a defect in the material modifies the expected radiation received by the sensor (Halmshaw, 1991). The phenomenon of differential absorption is illustrated in Fig. 3. The contrast in the X-ray image between an area containing a flaw and a defect-free area of the specimen allows distinguishing the flaw. We can see in an X-ray image that the defects, like voids, cracks or bubbles, show up as bright regions with respect to their neighbouring area. The reason is that the attenuation is smaller.

The absorption can be macroscopically modelled using the exponential attenuation law for X-rays (Kuchling, 1989; Halmshaw, 1991) as shown in Fig. 4:

$$\varphi(x) = \varphi_0 e^{-\mu x} \quad (1)$$

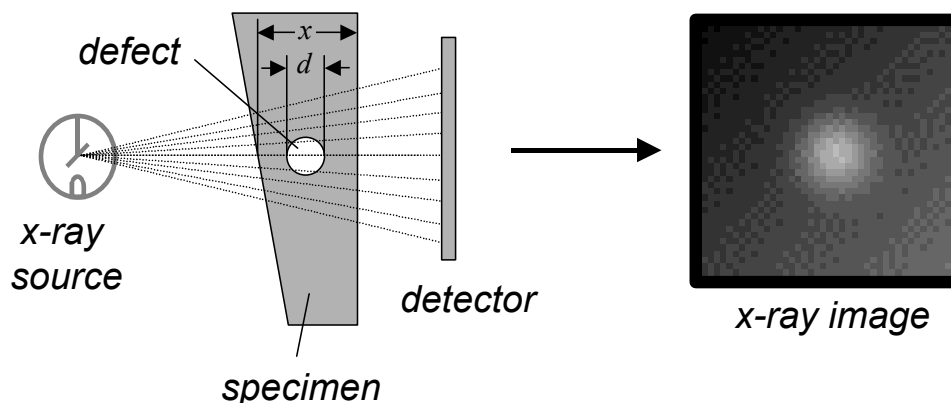


Fig. 3: Differential absorption in a specimen.

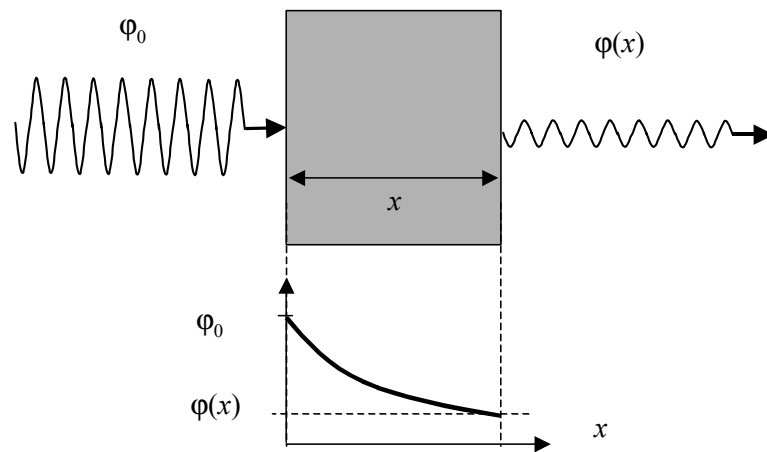


Fig. 4: Absorption law.

where  $\varphi_0$  is the incident radiation intensity,  $\varphi$  the transmitted intensity,  $x$  the thickness of the specimen (normally expressed in cm) and  $\mu$  is a constant known as the *linear absorption coefficient* of the material under test (with dimension  $\text{cm}^{-1}$ ). Coefficient  $\mu$  depends on the material and the X-ray energy. Figure 5 illustrates the linear absorption coefficient for aluminium plotted against X-ray energy. Typically, radioscopic testing of aluminium castings uses energy values between 50keV and 150keV (Hecker, 1996). In Fig. 5, the reader can find the values of  $\mu$  for this energy interval, in which  $\mu$  can be modelled as a fourth degree polynomial (Mery, 2001):

$$\mu \approx \sum_{i=0}^4 \theta_i E^i \text{ for } 50\text{keV} \leq E \leq 150\text{keV}, \tag{2}$$

with

$$\theta = [ 6.0 \quad -0.210 \quad -0.00304 \quad -1.97 \times 10^{-5} \quad 4.72 \times 10^{-8} ]^T$$

The grey value  $I$  registered by the CCD-camera can be expressed as a linear function of  $\varphi$ :

$$I(x) = A\varphi(x) + B, \tag{3}$$

where  $A$  and  $B$  are the linear parameters of  $I$ .

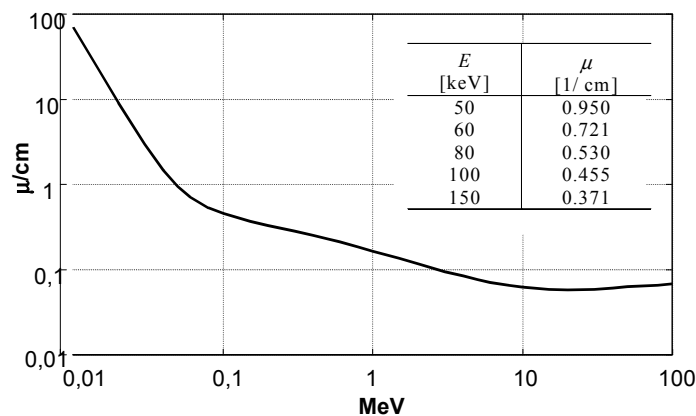


Fig. 5: Absorption coefficient  $\mu$  for aluminium against X

Now, we investigate what happens if the penetrated object has a cavity with thickness  $d$  as shown in Fig. 3. In this case, from (1) the transmitted radiation  $\varphi_d$  is given by:

$$\varphi_d = \varphi(x-d) = \varphi_0 e^{-\mu(x-d)} = \varphi(x) e^{\mu d}, \quad (4)$$

where we assume that the absorption coefficient of the cavity is zero. The grey value registered by the CCD camera is calculated then from (4) and (3) as:

$$I(x-d) = A\varphi(x) e^{\mu d} + B, \quad (5)$$

Substituting the value of  $A\varphi(x)$  from (3) we see that (5) may be written as:

$$I(x-d) = (I(x) - B) e^{\mu d} + B, \quad (6)$$

Parameter  $B$  can be estimated as follows: the maximal grey value  $I_{max}$  in a radioscopic image is obtained when the thickness is zero. Additionally, the minimal grey value  $I_{min}$  is obtained when the thickness is  $x_{max}$ . Substituting these values in (3), it yields:

$$B = I_{max} - \Delta I / (1 - e^{-\mu x_{max}}), \quad (7)$$

From these equations, we obtain that:

where  $\Delta I = I_{max} - I_{min}$ . Usually,  $I_{max}$  and  $I_{min}$  are 255 and 0 respectively. For these values,  $B$  can be written as:

$$B = 255 / (1 - e^{-\mu x_{max}}), \quad (8)$$

Using equation (6), we can alter the original grey value of the radioscopic image  $I(x)$  to simulate a new image  $I(x-d)$  with a flaw. A 3D flaw can be modelled, projected and superimposed onto a real radioscopic image. The new grey value of a pixel, where the 3D flaw is projected, depends only on four parameters: a) the original grey value  $I(x)$ ; b) the linear absorption coefficient of the examined material  $\mu$ ; c) the maximal thickness observable in the radioscopic image  $x_{max}$ ; and d) the length of the intersection of the 3D flaw with the modelled X-ray beam  $d$ , that is projected into the pixel. In the next Section we will describe how a 3D object is projected onto a radioscopic image.

### 3. Geometric Model

In this Section a model is presented, which describes the waypoints are going to be expressed from now on. It is important to understand that 2D points are used for the digital image pixels while 3D points will be used in the simulated 3D world.

In order to achieve this flaw-only simulation, it is necessary to remember the conditions in which the X-ray image was taken. This conditions include the focal distance  $f$  and the horizontal and vertical scale factors of the digital X-ray image  $K_u$  and  $K_v$ . It is also very important to be aware of the spots in which the simulated flaw will be "inside" the object. To make this parameters clear, the used coordinate systems will be explained.

**The 3D virtual world coordinate system:** This coordinate system has its origin in the centre of the simulated X-ray source, and though it is a virtual world 3D coordinate system, by assuming that the measurements are made with the same units, we can immediately translate the points to real world ones, this is, if the real world measurements were also taken from the X-ray source. A point of this coordinate system is denoted by

$$\mathbf{M} = [X \ Y \ Z]^T.$$

**The 2D digital image coordinate system:** In the X-ray image capture scheme, we can observe that the X-ray projective plane is always opposed to the X-ray source, leaving the specimen in-between both of them. To maintain this in the virtual world, the simulated X-ray projective plane is no more than a part of the  $Z = f$  plane which is pierced by the Z-axis. The conversion from this simulated X-ray projective plane to image pixels depends on the  $K_u$  and  $K_v$  parameters, which are respectively, the horizontal and vertical scale factor of the captured image measured in pixels per millimetre. Thus, if the digital image size is  $(x_{max}, y_{max})$  pixels, the virtual X-ray projective plane size is

$(x_{max}/K_u, y_{max}/K_v)$  millimetres and during the simulation process will be sampled every  $1/K_u$  millimetres horizontally and  $1/K_v$  vertically to produce a simulated digital image of the same dimensions of the real one. As shown in Fig. 6, a point  $m=(x,y)$  in the digital image is converted into

$$\mathbf{M} = \left[ \begin{array}{ccc} U_0 + x & V_0 - y & f \end{array} \right]^T$$

in the 3D virtual world coordinate system, where  $(U_0, V_0)$  is the origin of the simulated X-ray projective plane.

In the following Section, we will use these coordinate systems to explain how we produce a radiosopic image of flawed specimens by simulating only the flaw.

#### 4. Simulation of flaws

In order to simulate only the flaw and superimpose it onto a X-ray image, four steps need to be completed. First, it is necessary to capture a real X-ray digital image taking all the needed measurements, which include focal distance  $f$ , specimen dimensions and position, digital image scale factors  $K_u$  and  $K_v$  and digital image size  $(x_{max}, y_{max})$ . In the second step, the 3D flaw needs to be modelled as a 3D mesh. This is achieved using a 3D modelling software. The next step consists in positioning the 3D flaw in the virtual 3D space and simulate the X-ray capture process, obtaining a matrix that stores the length of the inner part of each ray that pierces the 3D flaw. This matrix is called the depth map, it is denoted by  $W(x,y)$  and its dimensions are  $(x_{max}, y_{max})$ . The last step consists in blending the depth map with the digital image according to equation (6).

In this paper, a flaw is modelled as a 3D mesh, which grants the ability to model complex flaws, including blowholes, cracks, voids, etc. Before explaining how to superimpose a flaw onto a X-ray image, it is important to understand what are 3D meshes and how they are stored and handled.

A 3D mesh is a 3D surface that is formed by polygons, which share, at least, one common side. A real world example of this is a soccer ball, which is formed by several leather patches in form of regular polygons, forming a sphere. Obviously, to form a pyramid with hexagonal patches would be difficult. This is why the standard 3D meshes are formed by the smallest polygon of all: the triangle. With triangles, any 3D surface can be modelled. If the 3D mesh is totally closed, it can resemble a volumetric object like a flaw, but it is important to know that the 3D mesh only represents the surface of it.

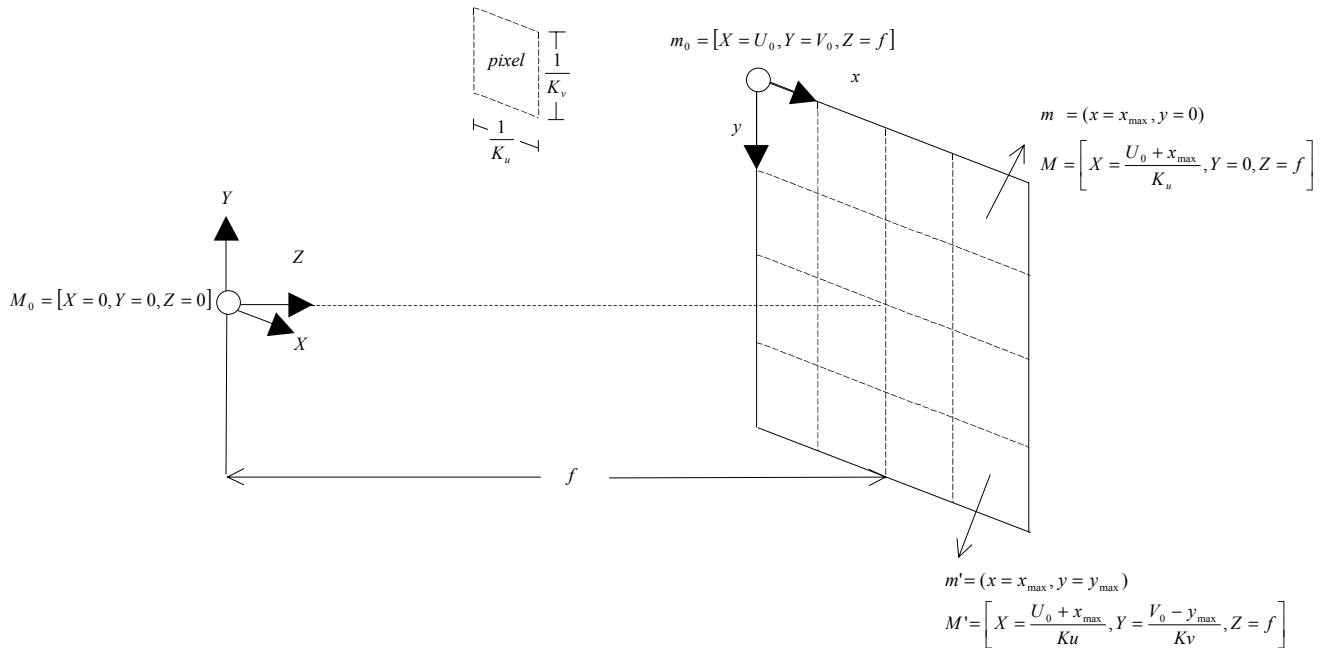


Fig. 6: Coordinate System Conversions.

3D meshes are stored in memory with *vertex lists* and *mesh lists*. The vertex list is a matrix that holds the coordinates for all the points that are vertices of at least one triangle of the mesh. This matrix is a  $n \times 3$  order matrix being  $n$  the number of vertices. The mesh list is a matrix that stores for each triangle, the 3 points that form them, its dimensions are  $m \times 3$ , where  $m$  is the number of triangles that form the mesh.

A 3D mesh is easily translated, rotated and scaled in the 3D virtual world by applying transformations to each vertex in the vertex list. This is very important during the simulation, because in this way, the flaw can be positioned in any place in the 3D virtual world, located in whatever orientation it is needed to be and scaled accordingly to the real flaw.

Another advantage of having the triangles stored as vertex and mesh lists rises when we need to check the existence and know the position of the intersection of a specific ray with a specific triangle. A ray is defined as a line in 3D virtual world coordinate system, and a point belonging to this line is parameterised by the scalar  $t$  as follows:

$$\mathbf{L}(t) = t \cdot \mathbf{D} + \mathbf{P} \quad (9)$$

where  $\mathbf{D} = [d_x \ d_y \ d_z]^T$  is the direction and  $\mathbf{P} = [p_x \ p_y \ p_z]^T$  is a known point belonging to the line. Triangles are also parameterised by the scalars  $u$  and  $v$  (see Fig. 7):

$$\mathbf{T}(u, v) = (1 - u - v) \cdot \mathbf{P}_0 + u \cdot \mathbf{P}_1 + v \cdot \mathbf{P}_2 \quad (10)$$

with the triangle vertices  $\mathbf{P}_0 = [p_{0x} \ p_{0y} \ p_{0z}]^T$ ,  $\mathbf{P}_1 = [p_{1x} \ p_{1y} \ p_{1z}]^T$ ,  $\mathbf{P}_2 = [p_{2x} \ p_{2y} \ p_{2z}]^T$ , and  $u \geq 0$ ,  $v \geq 0$ ,  $u + v \leq 1$ .

Matching (9) and (10), it yields:

$$\begin{aligned} t \cdot d_x + p_x &= (1 - u - v) \cdot p_{0x} + u \cdot p_{1x} + v \cdot p_{2x} \\ t \cdot d_y + p_y &= (1 - u - v) \cdot p_{0y} + u \cdot p_{1y} + v \cdot p_{2y} \\ t \cdot d_z + p_z &= (1 - u - v) \cdot p_{0z} + u \cdot p_{1z} + v \cdot p_{2z} \end{aligned} \quad (11)$$

Equation (11) yields to a  $3 \times 3$  linear equation system. If the obtained results satisfy restrictions (10), then a intersection is positioned at  $\mathbf{M} = t \cdot \mathbf{D} + \mathbf{P}$ .

Once the flaw is positioned, oriented and scaled, the next step is to find its depth map. A single ray is emitted from every pixel of the 2D digital image coordinate system to a random point of the spherical X-ray source, the distance inside the flaw is calculated and stored for each ray in a depth map cell. This is achieved by checking the intersection of the ray with every single triangle of the mesh. Typically, the ray should intersect a even number of triangles of the mesh, because as stated before, the mesh is supposed to be closed to correctly represent a volumetric flaw. Having the points where the ray intersected the triangles, the length of the portion of the ray that is inside the flaw can be calculated using Euclidean distance. This process, though effective, is not without drawbacks. Since floating-point numbers are used, precision rises as an important issue when it is needed to know if a particular intersection point is the same than other one. This usually happens in mesh intersections and vertices, because this areas always belong to more than one triangle. The general way to solve this is using a small delta value and instead of checking if both points are the same, the distance between them must be smaller than delta.

$$\mathbf{T}(u, v) = (1 - u - v) \cdot \mathbf{P}_0 + u \cdot \mathbf{P}_1 + v \cdot \mathbf{P}_2$$

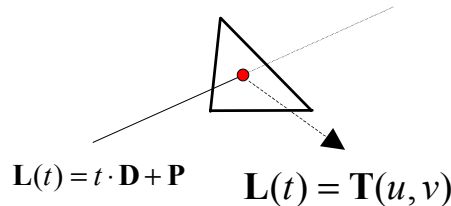


Fig. 7: Intersection of line with triangle.

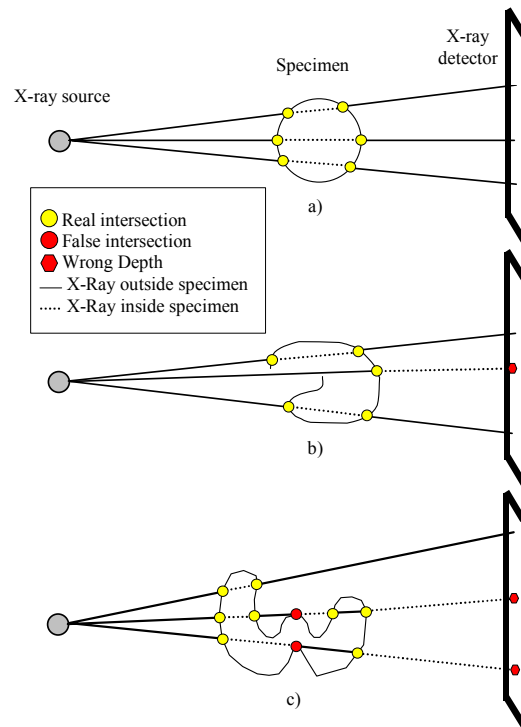


Fig. 8: Calculation of a specimen's depth map. a) Closed specimen, b) Open specimen, c) Error due to false intersections.

The final internal distance for every ray is calculated by sorting the points by distance to the 3D coordinate system origin and dismissing the equivalent points using the criteria explained above. Each intersection alternates the state of the ray from outside to inside and vice versa as shown in Fig. 8. The final depth stored is the sum of all the intern traces. The figure also shows the importance of identifying real intersections from bogus ones.

Another consideration needed to be made in order to correctly simulate a X-ray process is the fact that the detector is planar and not spherical, which means that the intensity of the X-rays is less in the corners of the detector than in the middle. A model to calculate the spatial correction factor is now explained.

A perfect X-ray detector would be a spherical one, this is because the distance of every ray to it would be virtually equal and the normal is parallel to the ray. Virtually, because the X-ray source is not punctual, but spherical which means that every ray could have a different origin, but always inside that sphere, making distances vary, though in small amounts. This simulation assumes the detector to be planar, so a spatial correction factor is needed. This factor is closely related to the solid angle of each pixel of the final image, so the proposed solution is to have a matrix with the same dimensions as the 2D digital image and store the solid angle of every pixel of it. The solid angle for any part of the  $Z=f$  plane is given by:

$$\Omega = \iint \frac{fdXdY}{\sqrt{(X^2 + Y^2 + f^2)^3}} \quad (12)$$

By integration we get:

$$\Omega(X_0, X_1, Y_0, Y_1, f) = \frac{|X| \cdot \tan^{-1} \left( \frac{X^2 Y}{|X| \cdot \sqrt{X^2 + Y^2 + f^2}} \right)}{X} \Bigg|_{X_0}^{X_1} \Bigg|_{Y_0}^{Y_1} \quad (13)$$



where  $X_0, X_1, Y_0$  and  $Y_1$ , are respectively the horizontal and vertical limits of the region of the  $Z=f$  plane for which the solid angle is required.

Now, another consideration needs to be made. As stated before, the detector used for this simulation is assumed to be planar, which implies that the solid angle will be maximum at the detector's origin (if detector and X-ray source are correctly aligned), decreasing by moving in any direction, which results in a pattern that resembles a set of concentric circles. Firstly, we set a correction factor  $C_f$  as follows:

$$C_f(X_0, X_1, Y_0, Y_1, f) = \frac{\Omega(X_0, X_1, Y_0, Y_1, f)}{4\pi} \quad (14)$$

This because the maximum value for solid angles is the value of the sphere surface, which is  $4\pi$ . The spatial correction needed for this simulation is a relation between the solid angle of the area of interest and the maximum solid angle. To set the maximum value for  $C_f$ , a constant  $\beta$  is used as follows.

$$C_f(-1,1,-1,1, f) \cdot \beta = 1 \quad (15)$$

which yields to

$$\beta = \frac{4\pi}{\tan^{-1}\left(\frac{1}{f\sqrt{2+f^2}}\right)} \quad (16)$$

resulting in

$$C_f(X_0, X_1, Y_0, Y_1, f) = \frac{\Omega(X_0, X_1, Y_0, Y_1, f)}{\tan^{-1}\left(\frac{1}{f\sqrt{2+f^2}}\right)}. \quad (17)$$

This spatial correction factor will apply over every pixel that has a corresponding depth map value greater than zero.

## 5. Experimental Results

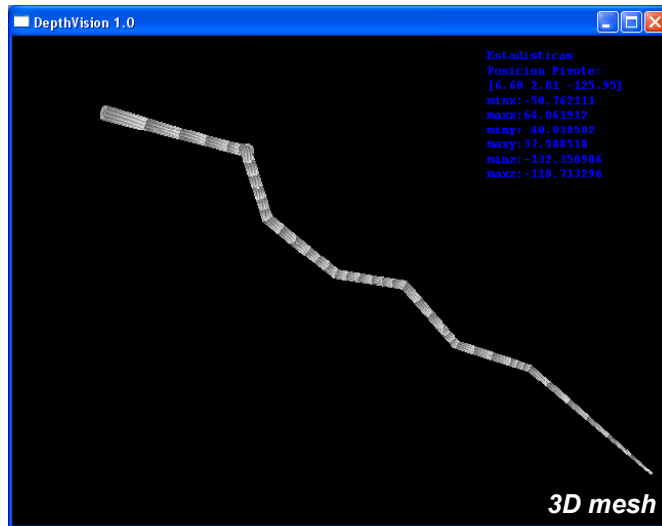
A program was developed to visualise, position, orient and scale a previously modelled 3D flaw at will as shown in figures  $x,y,z$ . The modelling process can be achieved using several 3D modelling programs available on the internet. Parameters include  $f, K_u, K_v$ , X-ray emitting sphere radius and image size. The output of this program is the associated depth map and spatial correction factor files. Screenshots, depth map visualisations and the respective simulated flaw can be observed in Fig. 9, where three cracks are simulated in different positions, and in Fig. 10, where blowholes using an ellipsoidal model are simulated.

Simulations in this Section were made on cast aluminium wheels using the approach outlined in the previous Section. The dimensions of the wheels used in our experiments were 47 cm diameter and 20 cm height approximately. The focal length was 884 mm.

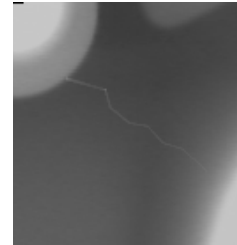
## 6. Summary

A new method for the simulation of defects in radioscopic images of aluminium castings has been presented. We propose an approach that simulates the flaws using a 3D polygonal mesh model, which is projected and superimposed onto real radioscopic images. The X-ray imaging process and the projection of a 3D object are discussed.

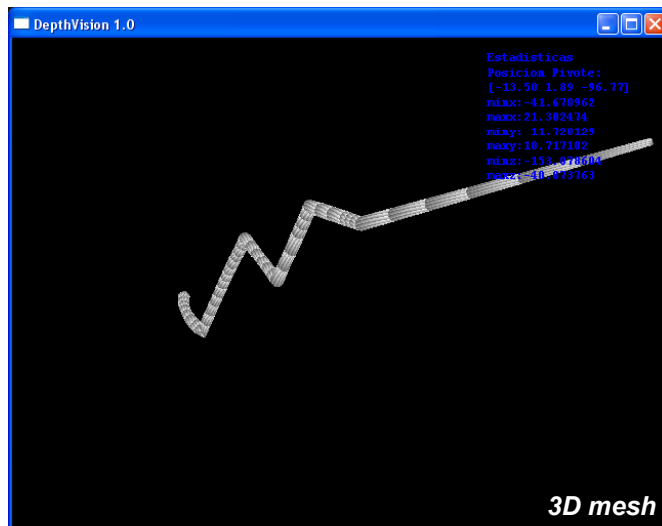
Using this tool a simulation of a complex geometry flaw of any size and orientation can be done in any position of the casting. This allows the precise evaluation of the performance of defect inspection systems in cases where the detection is known to be difficult.



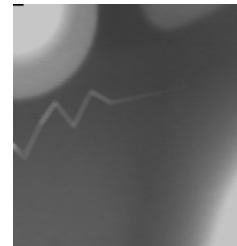
*Depth map*



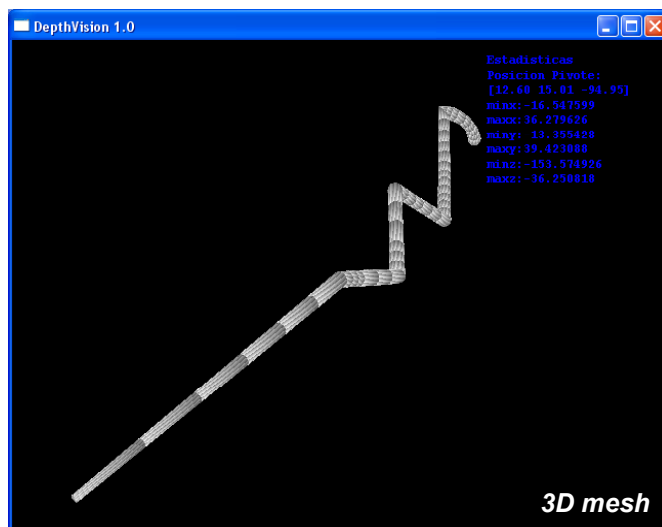
*Superimposing*



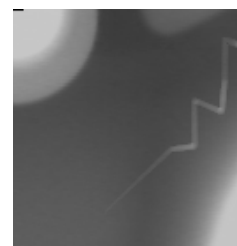
*Depth map*



*Superimposing*



*Depth map*



*Superimposing*

Fig. 9: A 3D mesh representing a crack superimposed in 3 different positions.

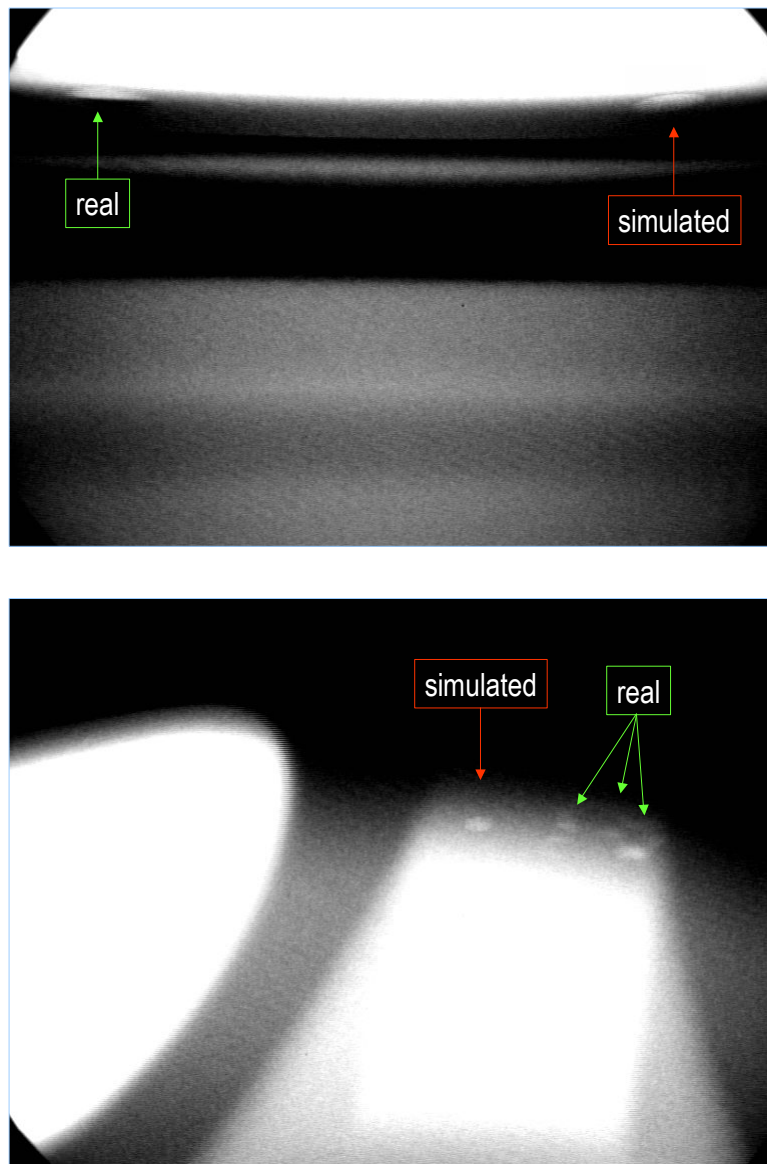


Fig. 10: Simulation of blow holes (Mery, 2001).

### Acknowledgements

The authors wish to thank the Department for Research and Development of the Universidad de Santiago de Chile (project DICYT 06-0119MQ) for financing this investigation, and the Technical University of Berlin for financing the participation in this Symposium.

### References

- K. Bavendiek: Prüfkörper für die Überprüfung der Bildqualität und der Messung der Erkennungssicherheit bei ADR System. In *Proceedings of the Jahrestagung der DGZfP 2001*, Berlin, 21.-23. Mai, 2001.
- H. Boerner and H. Strecker. Automated X-ray inspection of aluminum casting. *IEEE Trans. Pattern analysis and Machine Intelligence*, 10(1):79-91, 1988.
- D. Filbert, R. Klatt, W. Heinrich, and M. Purschke. Computer aided inspection of castings. In *Proceedings of the IEEE-IAS Annual Meeting*, pp. 1087-1095, Atlanta, USA, 1987.
- P. Freud, P. Duvauchelle, and D. Babot. Simulation of X-ray NDT imaging techniques. In *Proceedings of the 15th World Conference of Non-Destructive Testing (15th WCNDT)*, Rome, Oct, 15-21 2000.
- R. Halmshaw. *Non-Destructive-Testing*. Edward Arnold, London, 2 edition 1991.

- H. Hecker. *A new Method to Process X-ray Images in the Automated Inspection of Castings*. PhD thesis, Institute for Measurement and Automation, Faculty of Electrical Engineering, Technical University of Berlin, 1995. (in German).
- W. Heinrich. *Automated Inspection of Castings using X-ray Testing*. PhD thesis, Institute for Measurement and Automation, Faculty of Electrical Engineering, Technical University of Berlin, 1988. (in German).
- J.-M. Kosanetzky and H. Putzbach. Modern X-ray inspection in the automotive industry. In *Proceedings of the 14th World Conference of NDT (14th WCNDT)*, New Delhi, Dec 8-13 1996.
- H. Kuchling. *Taschenbuch der Physik*. Harri Deutsch, Thun-Frankfurt, Main, 12 edition, 1989.
- D. Mery. A new algorithm for flaw simulation in castings by superimposing projections of 3D models onto x-ray images. In *Proceedings of the XXI International Conference of the Chilean Computer Science Society (SCCC-2001)*, Punta Arenas, pp. 193-202, 6-8 Nov. 2001. IEEE Computer Society Press.
- D. Mery, T. Jaeger, and D. Filbert. Automated quality control of castings – state of the art. *tm – Technisches Messen*, 68(7-8), 2001. (in German).
- D. Mery and D. Filbert. Automated Flaw Detection in Aluminum Castings based on the Tracking of Potential Defects in a Radioscopic Image Sequence. *IEEE Trans. on Robotics and Automation*, 18(6): 890-901, 2002.
- G.R. Tillack, C. Nockemann, and C. Bellon. X-ray modelling for industrial applications. *NDT & E International*, 33(1):481-488, 2000.
- L. Westover. Footprint evaluation for volume rendering. In *Proceedings of SIGGRAPH*, 24(4):367-376, 1990.